POLITECNICO MILANO 1863

SCUOLA DI INGEGNERIA INDUSTRIALE E DELL'INFORMAZIONE

EXECUTIVE SUMMARY OF THE THESIS

Operation and Control Design of a Modular Multilevel Converter with Integrated Distributed Energy Resources under Unbalanced Grid Conditions

LAUREA MAGISTRALE IN ELECTRICAL ENGINEERING - INGEGNERIA ELETTRICA

Author: GABRIELE LISCACCI

Advisor: PROF. MARZIO BARRESI

Co-advisor: SIMONE BARCELLONA

Academic year: 2025-2026

1. Introduction

The transition toward low-carbon power systems is accelerating the penetration of renewable energy sources and progressively changing the operating conditions of electrical grids. Photovoltaic generation plays a central role in this transition, but its large-scale integration also increases the relevance of converter control. Modern grid-connected converters are no longer required only to inject active power: they must also guarantee current quality, support reactive-power regulation, and remain controllable during disturbances such as voltage unbalance.

In this context, modular multilevel converters (MMCs) represent an attractive solution because of their modularity, scalability, and high-quality voltage synthesis. In photovoltaic systems, their structure is especially promising because it allows the integration of energy sources directly at submodule level, supporting distributed maximum power point tracking (DMPPT). However, the same architecture introduces additional internal dynamics and the need for a more complex control strategy.

This thesis investigates the operation and control of a three-phase double-star chopper-cell MMC for photovoltaic applications under unbalanced grid conditions and non-uniform internal available power. The main goal is to design a control strategy capable of satisfying grid-side power objectives while at the same time redistributing power inside the converter so that the available arm powers imposed by DMPPT can be respected.

2. MMC-PV architecture and control problem

The considered system is a three-phase double-star chopper-cell MMC (Fig. 1) in which each phase-leg is composed of an upper and a lower arm, and each arm contains a series connection of half-bridge submodules interfaced with distributed PV sources.

For each phase-leg $j \in \{a, b, c\}$, the arm currents satisfy

$$i_{\mathrm{up},j} = i_{\mathrm{circ},j} + \frac{i_{ph,j}}{2}, \qquad i_{\mathrm{low},j} = i_{\mathrm{circ},j} - \frac{i_{ph,j}}{2}, \tag{1}$$

where $i_{ph,j}$ is the phase current injected into the grid and $i_{\mathrm{circ},j}$ is the circulating current inside the corresponding leg. Equation (1) highlights the key control insight of the thesis: the phase current is mainly responsible for the external power exchange, whereas the circulating current is the internal degree of freedom used to redistribute energy without directly modifying the terminal current.

Accordingly, the proposed strategy regulates the phase currents $i_{ph,j}$, the AC circulating-current components $i^{ac}_{\text{circ},j}$, and the DC circulating-current components $i^{dc}_{\text{circ},j}$ so as to satisfy both grid-side requirements and internal power-availability constraints. These quantities are ultimately controlled through suitable arm-level voltage references.

The AC circulating-voltage reference $v^{ac*}_{\text{circ},j}$, the DC circulating-voltage reference $v^{dc*}_{\text{circ},j}$ and the phase-voltage reference $v^{*}_{ph,j}$ generated by the controllers are then combined into the final upper- and lower-arm voltage references as follows:

$$v^*_{up,j} = -v^*_{ph,j} + \frac{1}{2}\left(V^*_{dc} - v^{dc*}_{\text{circ},j} - v^{ac*}_{\text{circ},j}\right), \quad (2)$$

$$v^*_{low,j} = \quad v^*_{ph,j} + \frac{1}{2}\left(V^*_{dc} - v^{dc*}_{\text{circ},j} - v^{ac*}_{\text{circ},j}\right). \quad (3)$$

3. Hierarchical control strategy

The proposed control architecture is structured in three coordinated layers based on PI controllers plus a final arm-voltage synthesis stage. The first layer is a dual-sequence grid controller. The second layer is an AC circulating-current controller devoted to vertical power transfers. The third layer is a DC circulating-current controller devoted to horizontal power transfers. The final stage combines the three voltage contributions and the DC-link voltage reference V^*_{dc} given by the DMPPT controller into upper- and lower-arm voltage references for the modulation and balancing layers.

3.1. Dual-sequence grid controller

The grid controller is responsible for regulating the power exchanged with the AC grid under both balanced and unbalanced operating conditions by acting on the positive- and negative-sequence injected currents. Under unbalanced grid voltage, positive- and negative-sequence components coexist and generate an oscillatory power term at twice the grid frequency. Therefore, the control problem is not simply to track active and reactive power references P^* and Q^*, but to decide how the oscillatory contribution is distributed among active and imaginary power. Specifically, the active-power reference is dictated by the PV-side available upper and lower arm powers $P^*_{\text{up},j}$ and $P^*_{\text{low},j}$ given by the DMPPT controller, such that

$$P^* = \sum_{j\in\{a,b,c\}} P^*_{\text{up},j} + \sum_{j\in\{a,b,c\}} P^*_{\text{low},j}. \quad (4)$$

The grid controller is designed in dual synchronous reference frames so that positive- and negative-sequence voltages $v^{\pm}_{g}$ and currents $i^{\pm}_{ph}$ can be processed separately as constant values in dq components. To this end, a PLL aligned with the positive-sequence grid voltage provides the angular reference for the $+\omega$ frame, while an auxiliary frame aligned with the negative-sequence grid voltage is secondly introduced.

The key analytical formulation governing the grid controller is the unified expression of the phase current references. Once the synchronous frames are aligned so that $v^+_{g,q} = v^-_{g,q} = 0$, the current references take the compact form

$$\begin{cases} i^{+*}_{ph,d} = \dfrac{2}{3}\,\dfrac{v^+_{g,d}P^*}{(v^+_{g,d})^2 + K(v^-_{g,d})^2}, \\ i^{+*}_{ph,q} = -\dfrac{2}{3}\,\dfrac{v^+_{g,d}Q^*}{(v^+_{g,d})^2 - K(v^-_{g,d})^2}, \\ i^{-*}_{ph,d} = \dfrac{2K}{3}\,\dfrac{v^-_{g,d}P^*}{(v^+_{g,d})^2 + K(v^-_{g,d})^2}, \\ i^{-*}_{ph,q} = \dfrac{2K}{3}\,\dfrac{v^-_{g,d}Q^*}{(v^+_{g,d})^2 - K(v^-_{g,d})^2}. \end{cases} \quad (5)$$

If $K = -1$, the controller suppresses the oscillatory term in active power. If $K = +1$, it suppresses the oscillatory term in imaginary power. If $K = 0$, the negative-sequence current is forced to zero and the converter injects balanced output currents even though both active and imaginary powers retain a 2ω oscillation.

A further relevant point addressed in the thesis concerns the difference between the imaginary power $Q = Q^+ - Q^-$ emerging from the adopted space-vector convention and the total reactive power $Q_T = Q^+ + Q^-$. When $K = \pm 1$, the injected negative-sequence current causes Q

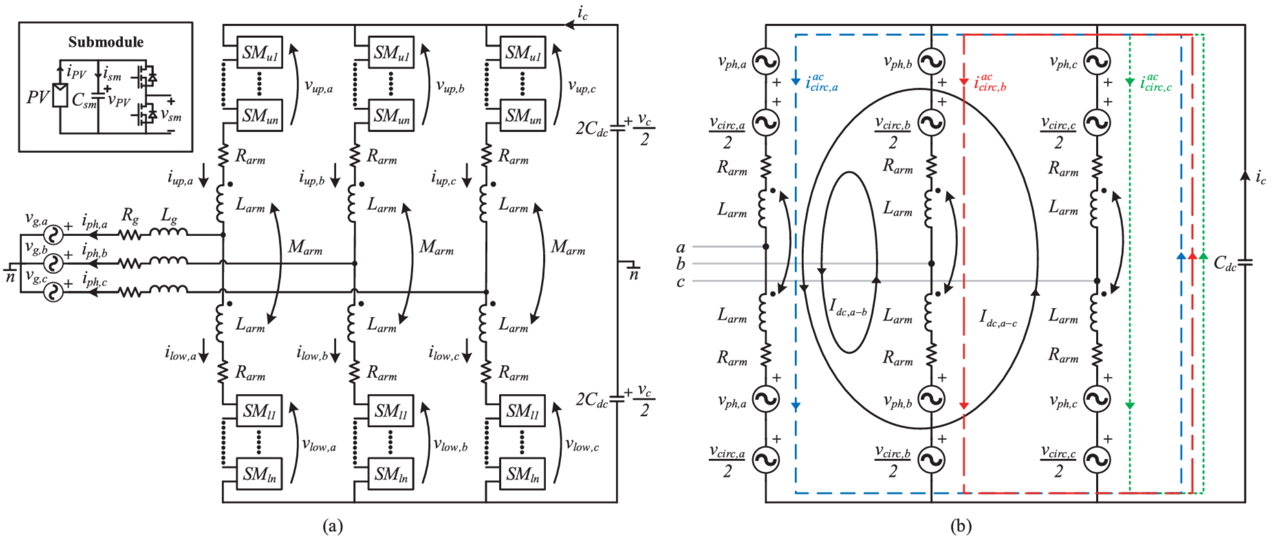

Figure 1: Converter topology for PV application: a) MMC three-phase; b) Equivalent circuit of the MMC.

Source: S. Barcellona, M. Barresi and L. Piegari, "MMC-Based PV Three-Phase System With Distributed MPPT," IEEE Transactions on Energy Conversion, vol. 37, no. 3, pp. 1567–1578, Sept. 2022. © 2022 IEEE

and Q_T to differ. For this reason, the thesis derives a formulation that converts the desired total reactive-power reference Q_T^* into the controller input Q^*, such that

$$Q^* = Q_T^* \frac{1 - K_v}{1 + K_v}, \qquad K_v \triangleq K \frac{{v_{g,d}^-}^2}{{v_{g,d}^+}^2} \tag{6}$$

Finally, an inner dual-sequence PI current regulator generates the converter-side phase-voltage reference v_{ph}^*.

3.2. AC circulating-current controller

The AC circulating-current controller is the control layer that manages the vertical mismatch, namely the mismatch between $P_{\text{up},j}^*$ and $P_{\text{low},j}^*$ within the same phase-leg j. Its purpose is to transfer active power between upper and lower arms so that each arm can operate at the available power level imposed by its local DMPPT condition. An indicator of vertical mismatch is defined as

$$P_{\text{diff},j}^* = P_{\text{up},j}^* - P_{\text{low},j}^*. \tag{7}$$

Instead of using a three-phase vector formulation, the thesis adopts three independent single-phase controllers, one for each leg. To construct the required single-phase synchronous frame, the phase-voltage reference $v_{ph,j}^*$ is processed by a single-phase PLL for each phase j.

The circulating current of the j-th leg is first decomposed into DC and AC parts. The DC component $i_{\text{circ},j}^{dc}$ is extracted by a moving average over one grid period T_g, while the fundamental AC component $i_{\text{circ},j}^{ac}$ is isolated by a band-pass filter centered at fundamental angular frequency ω. Through the Hilbert transform, an orthogonal signal is generated for $v_{ph,j}^*$ and $i_{circ,j}^{ac}$ to perform the Park transformation and express them in a dq frame aligned with the j-th phase voltage. In steady state, the differential active power can then be approximated by

$$\frac{P_{\text{diff},j}^*}{2} \approx \frac{1}{2} i_{\text{circ},d,j}\, v_{ph,d,j}^*, \tag{8}$$

which leads to the direct-axis circulating-current reference

$$i_{\text{circ},d,j}^* = \frac{P_{\text{diff},j}^*}{v_{ph,d,j}^*}, \qquad i_{\text{circ},q,j}^* = 0. \tag{9}$$

Only the in-phase component of the circulating current is required for differential active-power transfer, while the quadrature component is forced to zero to avoid internal reactive circulation and additional losses.

The tracking of these references is performed by three PI regulators that generate the AC circulating-voltage command $v_{\text{circ},j}^{ac*}$.

3.3. DC circulating-current controller and final coordination

The DC circulating-current controller compensates the horizontal mismatch among phase-legs. An indicator of horizontal mismatch is defined as

$$\Delta P^*_{ab} = (P^*_{\text{up},a} + P^*_{\text{low},a}) - (P^*_{\text{up},b} + P^*_{\text{low},b}). \tag{10}$$

The same method can be used to find the indicators ΔP^*_{ac} and ΔP^*_{bc}. This controller is needed not only when the available powers of the legs differ because of non-uniform irradiance, but also when the unbalanced grid causes the grid controller itself to impose a non-uniform phase-wise active-power split.

The thesis first derives the injected phase powers P_a^{inj}, P_b^{inj}, and P_c^{inj} from the selected grid operating mode, the positive- and negative-sequence voltages, and the power references P^* and Q^*. From these quantities, the injected unbalance indicators $\Delta P^{\text{inj}}_{ab}$, $\Delta P^{\text{inj}}_{ac}$ and $\Delta P^{\text{inj}}_{bc}$ are defined following the method showed in (10). The control objective is then to reconcile this injected power split with the available power split dictated by the PV sources. The required differential DC current references are obtained converting the mismatch between the injected active-power split and the available active-power split into DC circulating-current references as

$$I^*_{(a-b)} = \frac{\Delta P^{\text{inj}}_{ab} - \Delta P^*_{ab}}{V^*_{dc}}, \tag{11}$$

$$I^*_{(a-c)} = \frac{\Delta P^{\text{inj}}_{ac} - \Delta P^*_{ac}}{V^*_{dc}}. \tag{12}$$

It is worth noting that only two circulating-current references are needed due to the inherent constraint $\sum_{j\in\{a,b,c\}} i_{\text{circ},j} = 0$. After extracting $i^{dc}_{\text{circ},j}$, two PI regulators produce the differential DC circulating-voltage commands, that are finally mapped into the leg-wise voltage references $v^{dc*}_{\text{circ},j}$.

4. Simulation setup and considered scenarios

The proposed strategy is validated in time-domain simulation. Table 1 reports the key electrical parameters used in the simulations.

Table 1: Electrical parameters used in the time-domain simulations.

Parameter	Value
Grid fundamental frequency f_g	50 Hz
Positive-sequence grid voltage magnitude V_g^+	326.6 V
Positive-sequence phase displacement ϕ^+	0 °
Negative-sequence grid voltage magnitude V_g^-	65.3 V
Voltage unbalance ratio $\left(V_g^-/V_g^+\right)$	20 %
Negative-sequence phase displacement ϕ^-	30 °
DC-link voltage reference V^*_{dc}	783.8 V
Output resistance R_g	140 mΩ
Output inductance L_g	3.9 mH
Arm resistance R_{arm}	5 mΩ
Arm inductance L_{arm}	1 mH
Mutual arm inductance M_{arm}	0 mH
DC-bus capacitance C_{dc}	5 mF
Total Imaginary Power Reference Q^*_T	1 kvar

Two scenarios are considered. The first one isolates the effect of the grid-voltage unbalance by imposing identical available powers in all six arms. The second one is the most general operating condition investigated in the thesis, because it combines negative-sequence grid voltage with both vertical and horizontal power mismatch. The corresponding power references are summarised in Table 2.

Table 2: Simulation scenarios considered in the time-domain analysis.

	Case 1	Case 2
$P^*_{\text{up},a}$	1000 W	1000 W
$P^*_{\text{up},b}$	1000 W	600 W
$P^*_{\text{up},c}$	1000 W	1600 W
$P^*_{\text{low},a}$	1000 W	1000 W
$P^*_{\text{low},b}$	1000 W	1200 W
$P^*_{\text{low},c}$	1000 W	700 W
P^*	6000 W	6100 W

5. Results and discussion

5.1. Case 1: unbalanced grid with uniform available powers

Case 1 is intended to validate the dual-sequence grid controller in the absence of internal power mismatch. Since all arms are assigned the same available power, the AC circulating-current controller is not expected to produce any significant balancing action, whereas the DC circulating-current controller may still remain active because an unbalanced grid generally leads to a non-uniform phase-wise injected power split.

The results fully confirm the analytical behavior predicted by the selector K. For $K = -1$, the active-power oscillation is almost completely cancelled and the measured peak-to-peak ripple reduces to $\Delta P_{\text{pp}} = 4.95$ W, while the oscillatory content is transferred to the imaginary-power channel, with $\Delta Q_{\text{pp}} = 5068.65$ var. For $K = 0$, the converter injects balanced currents and both power channels show a 2ω oscillation, with $\Delta P_{\text{pp}} = 2433.48$ W and $\Delta Q_{\text{pp}} = 2432.96$ var. For $K = +1$, the opposite behavior is obtained: the imaginary-power ripple is nearly cancelled, $\Delta Q_{\text{pp}} = 4.00$ var, while the active-power ripple becomes dominant, $\Delta P_{\text{pp}} = 4679.12$ W.
Despite these different oscillatory behaviors, all three operating modes preserve accurate tracking of the average commands, with the average power values over two periods T_g at steady state being $\overline{P} \approx 6000.5$ W and $\overline{Q_T} \approx 1000.0$ var.
The current-level results are equally meaningful. The balanced-current mode $K = 0$ keeps the three phase currents almost equal, whereas $K = \pm 1$ intentionally introduce a negative-sequence current component. Moreover, the three-phase equivalent RMS phase current $i_{ph,3\phi}^{\text{rms}}$ shows that $K = +1$ yields the lowest grid-side RMS current, while $K = -1$ gives the highest one, leading to higher losses.
From the viewpoint of internal variables, the AC circulating-current RMS values remain practically zero in all legs, coherently with the null vertical mismatch references. The DC circulating-current controller, however, still generates non-zero steady-state offsets. This is due to the fact that, even without PV-side mismatch, the unbalanced grid operating point requires a leg-wise redistribution so that the phase-dependent injected power split can be achieved without violating the arm-level power requirements.

5.2. Case 2: unbalanced grid with arm and leg mismatch

Case 2 is the most representative operating condition of the thesis because both internal and external asymmetries are present simultaneously. The arm-level power references are not uniform, so the converter must enforce the vertical mismatch in legs b and c while also compensating the horizontal mismatch among the three legs.
The grid-side results show that, for $K = -1$, the active-power ripple remains nearly suppressed, with $\Delta P_{\text{pp}} = 4.95$ W, while the imaginary-power ripple rises to $\Delta Q_{\text{pp}} = 5151.10$ var. For $K = 0$, both quantities oscillate with comparable amplitude, $\Delta P_{\text{pp}} = 2473.05$ W and $\Delta Q_{\text{pp}} = 2472.53$ var. For $K = +1$, the imaginary-power ripple is again minimized, $\Delta Q_{\text{pp}} = 4.00$ var, and the active-power ripple becomes dominant, $\Delta P_{\text{pp}} = 4755.22$ W. In all modes, the average quantities remain accurately regulated around $\overline{P} \approx 6100.5$ W and $\overline{Q_T} \approx 1000.0$ var.
The current behavior is again consistent with the theory. The balanced-current mode $K = 0$ keeps the phase currents almost equal, while $K = \pm 1$ inject a controlled negative-sequence current and therefore produce phase-current asymmetry. The three-phase equivalent RMS phase current $i_{ph,3\phi}^{\text{rms}}$ confirms the same behavior observed in Case 1, showing that $K = +1$ yields the lowest grid-side RMS current, while $K = -1$ gives the highest one, leading to higher losses.
The most important results, however, concern the internal power-routing actions. Because $P_{\text{diff},a}^* = 0$, the AC circulating-current component in leg a stays negligible for all modes. In contrast, legs b and c develop substantial AC circulating-current RMS values, namely $i_{\text{circ},b}^{ac,\text{rms}} \approx 1.27$ A and $i_{\text{circ},c}^{ac,\text{rms}} \approx 2.28$ A, exactly as expected from the non-zero vertical mismatch references $P_{\text{diff},b}^* = -600$ W and $P_{\text{diff},c}^* = 900$ W. This confirms that the AC controller acts selectively where differential arm-to-arm transfer is required.
The DC circulating-current components are also more pronounced than in Case 1. Their steady-state values vary with K because the grid controller changes the phase-wise injected active-power split depending on the selected operating mode.
A particularly important outcome of the simulations is that the average arm powers converge to their individual references in all three K-modes. The tracking errors remain small compared with the commanded values: the largest deviation is below 12 W, which is less than about 1.2% of the corresponding arm power. Therefore, the controller does not merely regulate the total power at converter terminals, it also enforces the DMPPT-driven internal power distribution with good accuracy.
Tables 3–6 condense the most relevant results.

Table 3: Key grid-side steady-state metrics extracted from the simulations.

Measured quantity	K	Case 1	Case 2
$\overline{P}$ [W]	−1	6000.51	6100.52
	0	6000.51	6100.52
	+1	6000.50	6100.51
$\overline{Q_T}$ [var]	−1	1000.02	1000.02
	0	1000.03	1000.02
	+1	1000.03	1000.03
ΔP_{pp} [W]	−1	4.95	4.95
	0	2433.48	2473.05
	+1	4679.12	4755.22
ΔQ_{pp} [var]	−1	5068.65	5151.10
	0	2432.96	2472.53
	+1	4.00	4.00
$i_{ph,3\phi}^{\mathrm{rms}}$ [A]	−1	9.327	9.479
	0	8.780	8.923
	+1	8.610	8.750

Table 4: Measured arm active powers.

		Case 1			Case 2		
	K	−1	0	+1	−1	0	+1
P_{up} [W]	a	1000	1000	1000	1000	1000	1000
	b	1000	1000	1000	600	600	600
	c	1000	1000	1000	1600	1600	1600
P_{low} [W]	a	1000	1000	1000	1000	1000	1000
	b	1000	1000	1000	1200	1200	1200
	c	1000	1000	1000	700	700	700

Table 5: Steady-state RMS values of i_{circ}^{ac} [A].

Case	Phase	$K = -1$	$K = 0$	$K = +1$
1	a	7.9399e-05	3.2923e-04	6.4683e-04
	b	1.5841e-04	7.0932e-05	8.4332e-06
	c	7.9032e-05	4.0002e-04	6.4800e-04
2	a	8.7112e-05	3.3757e-04	6.5894e-04
	b	1.28109	1.26755	1.25529
	c	2.25352	2.28045	2.30569

Table 6: Steady-state values of i_{circ}^{dc} [A].

Case	Phase	$K = -1$	$K = 0$	$K = +1$
1	a	-0.088593	0.399425	0.849902
	b	0.177192	0.085041	-2.124e-05
	c	-0.088599	-0.484466	-0.849881
2	a	-0.0460668	0.449316	0.906593
	b	0.474873	0.382722	0.297659
	c	-0.428806	-0.832038	-1.204250

6. Conclusions

This thesis developed and validated a hierarchical control strategy for an MMC-based three-phase PV system with distributed energy resources integrated at submodule level under unbalanced grid conditions.

The first main contribution of this work is the formulation of a dual-sequence grid controller with three operating modes, parameterized by $K \in \{-1, 0, 1\}$, enabling a trade-off among active-power ripple suppression, balanced output currents, and imaginary-power ripple suppression. The second contribution is the formulation of two internal balancing functions based on circulating currents: a per-phase AC circulating-current controller for vertical arm balancing and a DC circulating-current controller for horizontal leg balancing.

The simulation results demonstrate that the proposed architecture achieves the intended objectives. In the absence of internal power mismatch, it reproduces exactly the expected selector-dependent trade-off under voltage unbalance. In the presence of both arm and leg mismatch, it maintains correct grid-side power regulation while generating the AC and DC circulating-current components required to enforce the prescribed internal power distribution. Finally, the arm powers converge to their respective available-power references, thereby confirming the correct operation of the proposed control law.

Overall, the thesis demonstrates that the proposed control architecture is a viable solution for MMC-based PV systems operating under unbalanced grid conditions and internal power mismatch.

References

[1] S. Debnath, J. Qin, B. Bahrani, M. Saeedifard, and P. Barbosa, "Operation, control, and applications of the modular multilevel converter: a review," *IEEE Transactions on Power Electronics*, vol. 30, no. 1, pp. 37–53, 2015.

[2] S. Barcellona, M. Barresi, and L. Piegari, "MMC-Based PV Three-Phase System With Distributed MPPT," *IEEE Transactions on Energy Conversion*, vol. 37, no. 3, pp. 1567–1578, 2022, doi: 10.1109/TEC.2022.3167786.

[3] S. Barcellona, M. Barresi, and L. Piegari, "MMC-Based PV Single-Phase System with Distributed MPPT," *Energies*, vol. 13, Art. no. 3964, 2020, doi: 10.3390/en13153964.